Discontinuous precipitation of Co_3V in a complex Co-based alloy

Ayan Bhowmik*, Kevin M. Knowles and Howard J. Stone

Department of Materials Science and Metallurgy, University of Cambridge,

27 Charles Babbage Road, Cambridge, CB3 0FS, UK

Abstract

Discontinuous precipitation of chromium-rich Co_3V lamellae has been found in a Co-based alloy containing 2 wt% V after prolonged ageing at 800 °C. This discontinuous precipitation is associated with a noticeable redistribution of alloying elements in the alloy relative to those parts of the aged alloy that preserve the c.c.p.–$L1_2$ microstructure found in the as-cast and homogenised condition. The orientation relationship between the c.c.p. Co-rich matrix and these hexagonal phase chromium-rich Co_3V precipitates is shown to be $[1\bar{1}0]_{Co} \parallel [100]_{Co_3V}$ and $[111]_{Co} \parallel [001]_{Co_3V}$, i.e. $[1\bar{1}0]_{Co} \parallel [2\bar{1}\bar{1}0]_{Co_3V}$ and $[111]_{Co} \parallel [0001]_{Co_3V}$ in the four-index notation. 3 × 3 transformation matrices relating directions and planes in the two phases have been established. The observed orientation relationship between the two phases is consistent with low lattice misfit between the two phases.

Keywords: ageing; cobalt; crystallography; precipitation; transmission electron microscopy (TEM)

* Corresponding author. *Tel.*: +44 (0) 1223 31950; *Fax*: +44 (0) 1223 331956
E-mail address: ab754@cam.ac.uk (Ayan Bhowmik)

1. Introduction

The nickel-based superalloys widely used in high temperature structural applications typically contain precipitates based on Ni_3Al embedded coherently within a nickel-rich solid solution matrix. The matrix is cubic close packed (c.c.p.) while the precipitates have the $L1_2$ crystal structure in the Strukturbericht notation. The exceptional properties derived from this microstructure enables current nickel-based superalloys to be used as components in the hot parts of gas turbines for thousands of hours, even allowing for the inevitable coarsening of the precipitate distribution during the service life of such components [1]. In order to make further improvements in the efficiency of gas turbine engines, considerable research continues to be conducted worldwide to develop new nickel-based superalloys and alloys based on alternative systems with increased temperature capability. Notable among the latter category are the alloys based upon cobalt.

Of the various $L1_2$ phases that may be exploited to strengthen a c.c.p. Co-based matrix, Co_3Ti has been studied by a number of workers. Polycrystalline Co_3Ti displays an anomalous increase of yield strength at around 600 °C [2], similar to Ni_3Al and a number of other ordered $L1_2$ intermetallic phases [2–4]. Early experiments on binary Co–Ti alloys containing 5 wt% and 9 wt% Ti by Blaise et al. produced two-phase c.c.p.–$L1_2$ microstructures successfully, in which the Co_3Ti $L1_2$ phase precipitated within the c.c.p. Co matrix in a cube–cube orientation relationship [5]. This orientation relationship arises as a consequence of the similar lattice parameters of the two phases, with a relatively low misfit of 1.26% [5], higher than the misfit found between γ and γ' in nickel-based superalloys [1]. For Blaise et al.'s work, alloys were prepared by solution heat treatment for 2 h at 1225 °C, followed by ageing at 700, 800 °C and 900 °C for up to 1000 h. Homogeneous precipitation of the $L1_2$ phase occurred in the 5 wt% Ti alloys heat-treated at 700 and 800 °C, while at 900 °C and above the solid solution did not decompose. However, in addition, a discontinuous lamellar pearlitic-type precipitation reaction was observed in these alloys at 700 °C, nucleating at grain boundaries. Homogeneous precipitation of the $L1_2$ phase occurred in the 9 wt% Ti alloys at all three temperatures, with additional discontinuous precipitation also occurring at both 700 and 800 °C.

In comparison with Ni_3Al, the solubility of alloying elements such as W, Mo and Cr in Co_3Ti is much lower, an exception being V, which actually has a higher solubility level in Co_3Ti than in Ni_3Al, substituting for Ti in the Co_3Ti structure [6,7]. When incorporated into

the Co_3Ti $L1_2$ crystal structure, Cr also substitutes for Ti [7,8]. This $L1_2$ phase is able to incorporate Co at the expense of Ti, so that the middle of the composition field is at Co – 23 at% Ti [7]; Cr can then be incorporated up to a level of 5 at%. By comparison, V can be incorporated into the $L1_2$ phase up to a level of at least 20 at% [7]. A consequence of the relatively poor solid solubility of many alloying elements in Co_3Ti is that it is not unlikely for a third phase to form in ternary Co–Ti–X alloys. Such alloys have also been shown to be prone to discontinuous reactions to relieve any supersaturation in the solid solution during prolonged thermal exposure; for example, this has been found in ternary Co–Ti alloys containing elements such as Ni, Mo, W and Ta [8].

Viatour et al. [8] also considered the effect of quaternary additions, X, in a series of Co–20Cr–5Ti–X alloys (in which the compositions were in wt%) for various transition metal elements. In such alloys, chromium is added to improve the oxidation resistance of the alloy. In ternary Co–20Cr–5Ti alloys, Viatour et al. observed that the Co_3Ti-based $L1_2$ γ' phase was produced as both a homogeneous precipitate and as a small amount of discontinuous reaction product, and that it was retained up to at least 900 °C. In compositions where X = 1.5, 2.5 or 5 wt% Mo, they reported homogeneous precipitation of the Co_3Ti-based $L1_2$ γ' phase and discontinuous precipitation of what they described as an ordered h.c.p. lamellar compound. However, structural details of this ordered compound were not given. In later work from the same group [9], it was noted that molybdenum can also act as a strengthener of the c.c.p. solid solution in cobalt-based alloys. Others workers have also observed that molybdenum can suppress discontinuous precipitation reactions in high cobalt austenitic alloys [10]. The possibility therefore arises of benefits being derived from a Co–20Cr–5Ti alloy with Mo additions, in which the Mo not only strengthens the cobalt-based c.c.p. solid solution, but also suppresses the discontinuous precipitation reaction.

In the work here, we have examined the microstructure produced in a Co–20Cr–5Ti–2.5Mo–2V alloy following a prolonged aging heat treatment. In this alloy, titanium and chromium were added at concentrations consistent with those examined by Viatour et al.. Molybdenum was added to provide solid solution strengthening, limit discontinuous precipitation and to increase the lattice parameter of the c.c.p. matrix. Molybdenum is known to partition preferentially to the c.c.p. matrix in nickel-based c.c.p.–$L1_2$ alloys [11]. If Co–Co_3Ti based alloys behave in an analogous manner to nickel-based alloys, the lattice misfit between the c.c.p. and $L1_2$ phases could be reduced to a level closer to that of existing nickel-based alloys, thereby helping preserve the coherency of the

interface between the two phases. In a similar vein, vanadium has been reported to reduce the lattice parameter of Co_3Ti [7]. Together with the known high solubility of vanadium in Co_3Ti [12], this offers the prospect of reducing the lattice misfit still further. Alloying with vanadium also has the added benefit of providing effective strengthening of Co_3Ti [13]. Hence, the alloy was designed with the aim of having a stable c.c.p.–$L1_2$ γ - γ' microstructure with low lattice misfit between the consistuent phases.

2. Experimental Procedure

An ingot of a Co-based alloy with a composition in wt% of Co–20Cr–5Ti–2.5Mo–2V was prepared by vacuum arc melting raw elements of at least 99.9 wt% purity. Homogenisation heat-treatment of the as-melted alloy was carried out at a temperature of 1180 °C in an evacuated glass ampoule to prevent oxidation of the sample. Sections of the homogenised ingot were aged further at 800 °C for 1000 h to ascertain the microstructural and thermodynamic stability of the alloy at this temperature. For microstructural investigation by transmission electron microscopy, 3 mm diameter discs machined out from slices of the aged samples were electropolished using a solution of 10 vol.% perchloric acid and 90 vol.% methanol at –5 °C. Bright field images and selected area diffraction patterns (SADPs) from the samples were obtained using a JEOL 200CX transmission electron microscope. High angle annular dark field (HAADF) imaging and elemental analyses of the phases by energy dispersive spectroscopy (EDS) were performed in addition on a Tecnai F20 field emission gun microscope operated in the scanning transmission electron microscopy (STEM) mode.

3. Results and Discussion

In the as-cast and subsequently homogenised condition, the microstructure of the alloy comprised of a uniform distribution of cuboidal $L1_2$ Co_3Ti precipitates within the c.c.p. Co-based matrix. Encouragingly, this was also true after short term ageing treatments for 16 h at either 700 °C or 800 °C [12]. Following the ageing treatment at 800 °C for 1000 h, a significant volume fraction (~ 0.5) of the alloy still had this form of microstructure. However, it was evident that there were some regions in which there was discontinuous precipitation.

Discontinuous precipitation reactions manifest as heterogeneous precipitation on grain

boundaries of the matrix material and concurrent migration of the grain boundaries [14], as Blaise et al. have also described in their work on Co–Ti alloys [5]. Since this discontinuous precipitation replaces the c.c.p.–$L1_2$ microstructure, which is associated with desirable mechanical properties, by a coarser microstructure (as is evident from Figure 1), it is generally regarded as being undesirable in alloys. Nevertheless, as Manna et al. have noted [14], discontinuous precipitation reactions are of interest in their own right in the context of moving boundary solid state reactions.

A micrograph showing an example of the lamellae formed through discontinuous precipitation in this Co-based alloy (identifed as region ‘A’) adjacent to a region of conventional uniform precipitation of $L1_2$ Co_3Ti within a c.c.p. matrix (identified as region ‘B’) is shown in Figure 1a, together with SADPs from these regions, Figure 1b to 1g. The series of SADPs from the <100>, <101> and <111> zones of the c.c.p. matrix from the region with a uniform dispersion of Co_3Ti precipitates is consistent with the expected c.c.p.–$L1_2$ cube-cube orientation relationship between the two phases (Figures 1b, 1d, 1e). The pattern of diffraction spots in Figure 1c from the discontinuous precipitation region is indistinguishable from the pattern of diffraction spots in Figure 1b, retaining the four-fold symmetry of the spot positions seen at 000 in Figure 1b. However, it is apparent that Figure 1e and Figure 1g have additional ‘superlattice’ reflections in comparison with Figure 1d and Figure 1f respectively. Dark field images taken from the c.c.p. matrix reflections showed evidence for a low density of interfacial defects between the matrix and the precipitate; an example is shown in Figure 2.

A representative HAADF-STEM micrograph, showing regions of the lamellar discontinuous reaction products and the original γ - γ′ microstructure, is shown in Figure 3a. A higher magnification image in the vicinity of the transition between the lamellar region (denoted as ‘A’) and γ - γ′ region (denoted as ‘B’) is shown in Figure 3b together with qualitative EDS maps of the Co, Ti, V, Cr and Mo concentrations. Arbitrary scaling of the data was applied to highlight the composition difference between the matrix and precipitates in both regions ‘A’ and ‘B’. It is apparent from Figure 3 that in region ‘A’, the precipitate is deficient in Ti, and has a noticeable Co, Cr and V content. By comparison, the matrix is richer in Ti and Mo. Within region ‘B’, the elemental distribution between the c.c.p. matrix and $L1_2$ Co_3Ti shows the latter to be rich in Co and Ti and lean in Cr and V, in comparison with the c.c.p. matrix. Interestingly, the c.c.p. matrix in equilibrium with Co_3V (in ‘A’) and Co_3Ti (in ‘B’), have different chemical compositions, with a higher Co-content in the former

than the latter. This suggests significantly different elemental partitioning behaviours between these two-phase systems.

The electron diffraction spots in Figures 1c, 1e and 1g can all be indexed to the hexagonal Co_3V phase, into which Cr has evidently partitioned preferentially. This *hP*24 phase (in Pearson notation) is the stable phase in the Co–V system below 1045 °C for a composition of Co–25 at%V [14]. Significantly, this phase has a relatively wide composition field in the Co–V system from 22 at% V to 32 at% V [16]. Recent work on the Co–Cr–V ternary system has shown that at 800 °C up to 15 at% Cr can be incorporated into this phase [17].

The structure of Co_3V was established by Saito [18] as being an ordered close-packed hexagonal phase with a = 5.032 Å and c = 12.27 Å. Saito deduced that the space group of this phase was $P\bar{6}m2$. However, reanalysis of the structure proposed by Saito shows that it is actually centrosymmetric with space group $P6_3/mmc$ [19] and that, as a consequence, Co_3V is isostructural with γAl_3Pu [20,21]. In the description of the atomic positions given by Saito [18], there are centres of symmetry at (0,0,$^1/_4$) and (0,0,$^3/_4$); shifting the origin to one of these centres of symmetry enables the descriptions of the atomic positions of γAl_3Pu given by Larson et al. [20] to be used for Co_3V. This structure has a six-layer repeat *abcacb* stacking sequence of the (001) planes.

Above 1070 °C, Co_3V is known to undergo a disordering reaction to the c.c.p. structure. Saito noted that the lattice parameter of this c.c.p. phase obtained at room temperature from quenched samples of Co_3V alloys following homogenisation at 1175 °C was a_c = 3.55 Å. This lattice parameter and those of the ordered hexagonal phase are approximately equated by $a = \sqrt{2}a_c$ and $c = 2\sqrt{3}a_c$, indicating the atomic arrangements in these structures are closely related.

For hexagonal materials for which $a = \sqrt{2}a_c$ and $c = 2\sqrt{3}a_c$ the interplanar spacings, d_{hkl}, of the *hkl* planes will conform to the formula

$$d_{hkl}^2 = \frac{12a_c^2}{8(h^2 + k^2 + hk) + l^2} \qquad (1)$$

so that, for example,

$$d_{102} = d_{1\bar{1}\bar{2}} = a_c \quad \text{and} \quad d_{2\bar{1}0} = d_{014} = \frac{a_c}{\sqrt{2}} \qquad (2)$$

i.e., the superlattice spots in Figure 1c closest to 000 can be indexed in a self-consistent manner. Therefore, even though there would appear to be a four-fold symmetry present in Figure 1c from the precipitate part of region ‘A’, this is explicable in terms of the close relationship of the Co_3V ordered close-packed hexagonal phase to the Cu_3Au-type $L1_2$ structure noted by Saito [18].

A further check that this is a possible indexing scheme for Figure 1c is to confirm that the interplanar angles are consistent with expectations. For $a = \sqrt{2}a_c$ and $c = 2\sqrt{3}a_c$, the angle between two hexagonal planes with indices (*hkl*) and (*h'k'l'*) is 90° if

$$8\,(hh' + kk' + \tfrac{1}{2}\,(hk' + kh')) + ll' = 0 \qquad (3)$$

and it is evident that this is satisfied for both (i) (102) and $(1\bar{1}\bar{2})$ and (ii) $(2\bar{1}0)$ and (014) in Figure 1c. Hence, the parallel zone axes in Figure 1c from the two distinct parts of region ‘A’ are $[001]_{Co} \parallel [\bar{2}\bar{4}1]_{Co_3V}$. Similarly, Figure 1e and Figure 1g can be identified as the zones $[101]_{Co} \parallel [1\bar{1}1]_{Co_3V}$, and $[111]_{Co} \parallel [001]_{Co_3V}$ respectively.

A consideration of the orientation relationships in Figures 1c, 1e and 1g shows that they are special cases of the orientation relationship

$$\begin{aligned} [1\bar{1}0]_{Co} &\parallel [100]_{Co_3V} \\ [01\bar{1}]_{Co} &\parallel [010]_{Co_3V} \\ [111]_{Co} &\parallel [001]_{Co_3V} \end{aligned} \qquad (4)$$

between the c.c.p. Co-rich lamellae and the Co_3V lamellae within the discontinuous reaction product.

A region of discontinuous precipitation adjacent to the one imaged in Figure 1 is shown in Figure 4a, together with its electron diffraction pattern in Figure 4b. It is evident that Figure 4b can be labelled as $[1\bar{1}0]_{Co} \parallel [100]_{Co_3V}$, with the ‘polytype’ reflections from the Co_3V phase clearly evident parallel to the 111 reciprocal lattice direction of the c.c.p. matrix. It is also apparent that the interface between the c.c.p. Co-rich matrix and Co_3V is $(111)_{Co} \parallel (001)_{Co_3V}$ and that there is evidence for faulting parallel to this interface plane in the two phases.

The orientation relationship established in Equation (4) is reasonable and consistent with low misfits between the two phases. It is the same as that reported by Viatour et al. between discontinuous lamellar-type precipitates with the $D0_{24}$ structure with a two sequence *ab* repeat along [001] and the c.c.p. matrix in a Co–30wt%Ni–7wt%Ti alloy [8]. If we take the lattice parameter of the Co-rich lamellae as 3.554 Å, consistent with the value for Co – 20

at% Cr quoted by Ishida and Nishizawa in their evaluation of the Co–Cr phase diagram [22], then the fractional lattice misfits along the $<100>_{Co_3V}$ and $[001]_{Co_3V}$ directions are

$$\frac{5.032-3.554\sqrt{2}}{3.554\sqrt{2}} \text{ and } \frac{12.27-2\times3.554\sqrt{3}}{2\times3.554\sqrt{3}}$$

respectively, i.e. very low misfits of +0.117% and –0.336% respectively. This is consistent with the observation in Figure 2 of a low density of interfacial defects at the interfaces between the c.c.p. Co-rich lamellae and the Co_3V lamellae.

The misfits of +0.117% and –0.336% are so low that it is reasonable to construct 3 × 3 transformation matrices relating directions and planes in the two phases on the assumption that $a=\sqrt{2}a_c$ and $c=2\sqrt{3}a_c$. Using the formalism in Appendix 4 of [23], indices $[uvw]_{Co}$ and $[UVW]_{Co_3V}$ of parallel vectors of the same length in the two phases are related to one another through the formulae

$$\begin{bmatrix}u\\v\\w\end{bmatrix}_{Co}=\begin{bmatrix}1&0&2\\\bar{1}&1&2\\0&\bar{1}&2\end{bmatrix}\begin{bmatrix}U\\V\\W\end{bmatrix}_{Co_3V} \text{ and } \begin{bmatrix}U\\V\\W\end{bmatrix}_{Co_3V}=\frac{1}{6}\begin{bmatrix}4&\bar{2}&\bar{2}\\2&2&\bar{4}\\1&1&1\end{bmatrix}\begin{bmatrix}u\\v\\w\end{bmatrix}_{Co} \quad (5)$$

Similarly, indices $(hkl)_{Co}$ and $(HKL)_{Co_3V}$ of parallel planes are related to one another through the formulae

$$\begin{pmatrix}h\\k\\l\end{pmatrix}_{Co}=\frac{1}{6}\begin{pmatrix}4&2&1\\\bar{2}&2&1\\\bar{2}&\bar{4}&1\end{pmatrix}\begin{pmatrix}H\\K\\L\end{pmatrix}_{Co_3V} \text{ and } \begin{pmatrix}H\\K\\L\end{pmatrix}_{Co_3V}=\begin{pmatrix}1&\bar{1}&0\\0&1&\bar{1}\\2&2&2\end{pmatrix}\begin{pmatrix}h\\k\\l\end{pmatrix}_{Co} \quad (6)$$

Hence, the four symmetrically related zone axes $[111]_{Co}$, $[\bar{1}11]_{Co}$, $[1\bar{1}1]_{Co}$ and $[11\bar{1}]_{Co}$ are parallel to $[001]_{Co_3V}$, $[\bar{8}\bar{4}1]_{Co_3V}$, $[4\bar{4}1]_{Co_3V}$ and $[481]_{Co_3V}$ respectively.

The $[111]_{Co} \parallel [001]_{Co_3V}$ electron diffraction pattern is of further interest. In his description of the crystal structure of Co_3V, Saito [18] noted that all the reflections for which $h – k = 3n$ and $l \neq 6n$ or $h – k \neq 3n$ and $l = 6n$ are missing from the X-ray diffraction pattern, i.e. in terms of electron diffraction, they are kinematically forbidden. Hence, on this basis, reflections such as 100, 200, 010 and 020 from Co_3V are forbidden reflections. However, it is evident from Figure 1g that these are clearly present in the electron diffraction pattern from $[111]_{Co} \parallel [001]_{Co_3V}$. In particular, the 200 and 400-type Co_3V reflections are noticeably strong. A series of dark field images from $\mathbf{g} = 200_{Co_3V}$, $\mathbf{g} = 400_{Co_3V}$ and $\mathbf{g} = 600_{Co_3V}$ taken away from the [001] zone are shown in Figure 5. These show that the 200_{Co_3V} and 400_{Co_3V} reflections do not disappear and that the dark field images from these reflections are very

strong in intensity. The 600_{Co_3V} reflection is coincident with the $4\bar{2}\bar{2}_{Co}$ reflection, and so for this reflection both the c.c.p. Co-rich matrix and the Co_3V lamellae are shown bright in the corresponding dark field image.

The ideal stoichiometric Co_3V crystal structure has V atoms in sites 2*b* and 4*f* and Co atoms in sites 6*h* and 12*k* (Table 1). For reflections with or $h - k \neq 3n$ and $l = 6n$, the atoms on the 2*b* and 4*f* sites scatter exactly out of phase with one another, as do those on the 6*h* and 12*k* sites. Hence, for this ideal crystal structure, reflections such as 100, 200 and 400 have zero structure factors. However, as we have noted previously, the Co_3V phase field extends along the Co–V line and also into the ternary Co–Cr–V phase region [16,17]. Therefore, any departure in exact chemistry between the 2*b* and 4*f* sites, and/or between the 6*h* and 12*k* sites will enable these reflections to have non-zero structure factors.

The observation of only c.c.p. Co and Co_3V in the discontinuous precipitation reaction product rather than c.c.p. Co, h.c.p. Co and Co_3V expected in the ternary Co–Cr–V system [17] may be rationalised by the stabilising effect of titanium on the c.c.p. Co polytype reported in the Co–Ti binary system [24]. However, this requires that the stabilising effect of titanium on the c.c.p. Co polytype dominates over the destabilising effect that may be expected with molybdenum additions from the Co–Mo binary phase diagram [25].

In terms of classification of discontinuous precipitation reactions, the reaction in this Co–Cr–Ti–Mo–V alloy is one which can be termed Type 3 [26,27], i.e. of the generic form

$$\alpha' + \beta \rightarrow \alpha + \delta$$

in which the coherent, metastable β precipitates are precursors to the thermodynamically stable δ phase. It is evident that the discontinuous precipitation reactions identified by Viatour et al. [8] in ternary and quaternary cobalt-base alloys are also Type 3, since the $D0_{19}$ and $D0_{24}$ ordered hexagonal compounds they found as a result of the discontinuous precipitation reaction have crystal structures different from that of the initial $L1_2$ Co_3Ti precipitates. In the example of Type 3 discontinuous precipitation that we have found here, there is a noticeable difference in chemistry between the original $L1_2$ coherent $Co_3(Ti,V)$ metastable precipitate and the thermodynamically stable Cr-doped Co_3V precipitate.

4. Conclusions

Although the alloy under consideration did not prove to have a stable c.c.p.–$L1_2$ γ - γ′ microstructure, the specifics of the discontinuous precipitation observed in this alloy after long term ageing proved to be interesting microstructurally. This discontinuous precipitation is associated with a noticeable redistribution of alloying elements in the alloy relative to those parts of the aged alloy which preserve the c.c.p.–$L1_2$ γ - γ′ microstructure found in the as-cast and homogenised condition. In these parts, Cr and Mo segregated preferentially to the c.c.p. γ matrix, while the $L1_2$ γ′ precipitates were essentially $Co_3(Ti,V)$.

The precipitates that formed in the discontinuous precipitation were a hexagonal Cr-rich Co_3V phase with a six-layer *abcacb* stacking scheme of the (001) planes. Cr substitutes into this phase so that reflections with $h - k \neq 3n$ and $l = 6n$, which would have zero structure factors in stoichiometric Co_3V, have finite structure factors in Cr-rich Co_3V. Ti rejected by this phase is incorporated into the Co-rich c.c.p. solid solution matrix component of the discontinuous precipitation. Mo remains as a solid solution strengthener of the c.c.p. matrix.

The orientation relationship between the c.c.p. Co-rich matrix and these hexagonal Cr-rich Co_3V precipitates was $[1\bar{1}0]_{Co} \parallel [100]_{Co_3V}$ and $[111]_{Co} \parallel [001]_{Co_3V}$, i.e. $[1\bar{1}0]_{Co} \parallel [1\,1\,\bar{2}\,0]_{Co_3V}$ and $[111]_{Co} \parallel [0001]_{Co_3V}$ in the four-index notation. 3×3 transformation matrices relating directions and planes in the two phases have been established and confirmed by an analysis of a number of electron diffraction patterns. The observed orientation relationship between the two phases is consistent with low lattice misfit between the two phases.

Acknowledgements

The authors are grateful to Dr J.P. Minshull for the alloy fabrication, homogenisation and ageing work. We would also like to acknowledge the EPSRC/Rolls-Royce plc Strategic Partnership (EP/H500375/1) for funding this work.

References

[1] R.C. Reed, Superalloys, Cambridge University Press, 2006.

[2] R.G. Davies and N.S. Stoloff, Trans. AIME 233 (1965) p.714.

[3] P.H. Thornton and R.G. Davies, Metall. Trans. 1 (1970) p.549.

[4] D.-M. Wee, O. Noguchi, Y. Oya and T. Suzuki, Trans JIM 21 (1980) p.237.

[5] J.M. Blaise, P. Viatour and J.M. Drapier, Cobalt 49 (1970) p.192.

[6] S. Ochiai, Y. Oya and T. Suzuki, Acta Metall. 32 (1984) p.289.

[7] Y. Liu, T. Takasugi and O. Izumi, Metall. Trans. A 17 (1986) p.1433.

[8] P. Viatour, J.M. Drapier, and D. Coutsouradis, Cobalt 1973·3 (1973) p.67.

[9] D. Coutsouradis, A. Davin and M. Lamberigts, Mater. Sci. Engng. 88 (1987) p.11.

[10] R.W. Guard and T.A. Prater, Transactions ASM 49 (1957) p.842.

[11] O. Kubaschewski, Ternary Alloys, VCH, Vol. 7, (1993) p 199.

[12] J.P. Minshull, Ph.D. thesis, University of Cambridge, Ch. 4 (2010).

[13] Y. Liu, T. Takasugi, O. Izumi and H. Suenaga, J. Mater. Sci. 24 (1989) p.4458.

[14] I. Manna, S.K. Pabi and W. Gust, Int. Mater. Rev. 46 (2001) p.53.

[15] G.J. Dickins, A.M.B. Douglas and W.H. Taylor, Acta Cryst. 9 (1956) p.297.

[16] L.J. Nagel, B. Fultz and J.L. Robertson, J. Phase Equil. 18 (1997) p.21.

[17] C.C. Zhao, Y.Yu, X.J. Liu and C.P. Wang, J. Phase Equil. and Diffusion 33 (2012) p. 189.

[18] S. Saito, Acta Cryst. 12 (1959) p.500.

[19] ICSD database, cif file 102718, Fachinformationszentrum Karlsruhe, accessed 1 July 2013.

[20] A.C. Larson, D.T. Cromer and C.K. Stamburgh, Acta Cryst. 10 (1957) p.443.

[21] H. Okamoto, J. Phase Equil. Diff. 30 (2009) p.293.

[22] K. Ishida and T. Nishizawa, Binary Alloy Phase Diagrams, 2nd Ed., Ed. T.B. Massalski 2 (1990) p. 1179.

[23] A. Kelly and K.M. Knowles, Crystallography and Crystal Defects, 2nd edition, Wiley, 2012.

[24] H. Okamoto, J. Phase Equilib. 22 (2001) p. 592.

[25] R. H. Lamoreaux, and L. Brewer, Binary Alloy Phase Diagrams, 2nd Ed., Ed. T.B. Massalski, 2 (1990) p. 1208.

[26] D.B. Williams and E.P. Butler, Int. Met. Rev. 3 (1981) p.153.

[27] M.N. Thompson, Ph.D. thesis, University of Cambridge, p.88 (1971).

Figure Captions

Figure 1. (a) Bright field TEM microstructure showing adjacent regions of Co-Co_3V lamellae ('A') and precipitation of Co_3Ti within the Co-rich matrix ('B'). Selected area diffraction patterns (b, d, f) from 'B' and (c, e, g) from 'A' respectively showing superimposed (b) $[001]_{Co} \parallel [001]_{Co_3Ti}$, (c) $[001]_{Co} \parallel [\overline{2}\overline{4}1]_{Co_3V}$, (d) $[101]_{Co} \parallel [101]_{Co_3Ti}$, (e) $[101]_{Co} \parallel [1\bar{1}1]_{Co_3V}$, (f) $[111]_{Co} \parallel [111]_{Co_3Ti}$ and (g) $[111]_{Co} \parallel [001]_{Co_3V}$ zone axes. The indices in normal, italics and underlined lettering correspond to Co, Co_3Ti and Co_3V respectively.

Figure 2 Dark field image from the c.c.p. component of the Co-Co_3V lamellae clearly showing a low density of interfacial defects at the Co/Co_3V interfaces, as well as dislocations in the c.c.p. phase.

Figure 3. (a) HAADF-STEM image of an area in which the Co–Co_3Ti c.c.p.–$L1_2$ microstructure coexists with the Co–Co_3V lamellar aggregate and (b) a magnified HAADF-STEM image of a region in the vicinity of the transition between and Co–Co_3V (denoted as 'A') and Co–Co_3Ti (denoted as 'B') together with qualitative EDS maps of elemental distributions from this region. The indices in normal, italics and underlined lettering correspond to Co, Co_3Ti and Co_3V respectively.

Figure 4 (a) Alternate lamellae of Co and Co_3V viewed down the $[1\bar{1}0]_{Co}$ and $[001]_{Co_3V}$ directions from one of the colonies adjacent to that shown in Figure 1. The selected area diffraction pattern suggest the interface plane between the two lamellae is $(111)_{Co} \parallel (001)_{Co_3V}$. Narrow planar faults on $(111)_{Co}$ and $(001)_{Co_3V}$ are evident in the two phases. (b) Electron diffraction pattern from (a) showing prominent spots from the $[1\bar{1}0]_{Co}$ and $[001]_{Co_3V}$ zone axes. The indices in normal and underlined lettering correspond to Co and Co_3V respectively.

Figure 5 (a) Selected area diffraction pattern showing the 200_{Co_3V}, 400_{Co_3V} and 600_{Co_3V} reflections from the Co–Co_3V aggregate. The 600_{Co_3V} reflection is coincident with the $4\bar{2}\bar{2}_{Co}$ reflection. The 200_{Co_3V} and 400_{Co_3V} are forbidden reflections in

stoichiometric Co_3V. (b)–(d): a series of selected area dark field images obtained using (b) $\mathbf{g} = 200_{Co_3V}$, (c) $\mathbf{g} = 400_{Co_3V}$ and (d) $\mathbf{g} = 600_{Co_3V}$. The bright lamellae in (b) and (c) are the Co_3V phase.

Table 1

Idealised atomic positions for Co_3V using the unit cell for γAl_3Pu given by Larson et al. [20]

Label	Multiplicity	Wyckoff letter	x	y	z
Co_1	6	h	$\frac{1}{2}$	0	$\frac{1}{4}$
Co_2	12	k	$\frac{1}{6}$	$\frac{1}{3}$	$\frac{7}{12}$
V_1	2	b	0	0	$\frac{1}{4}$
V_2	4	f	$\frac{1}{3}$	$\frac{2}{3}$	$\frac{1}{12}$

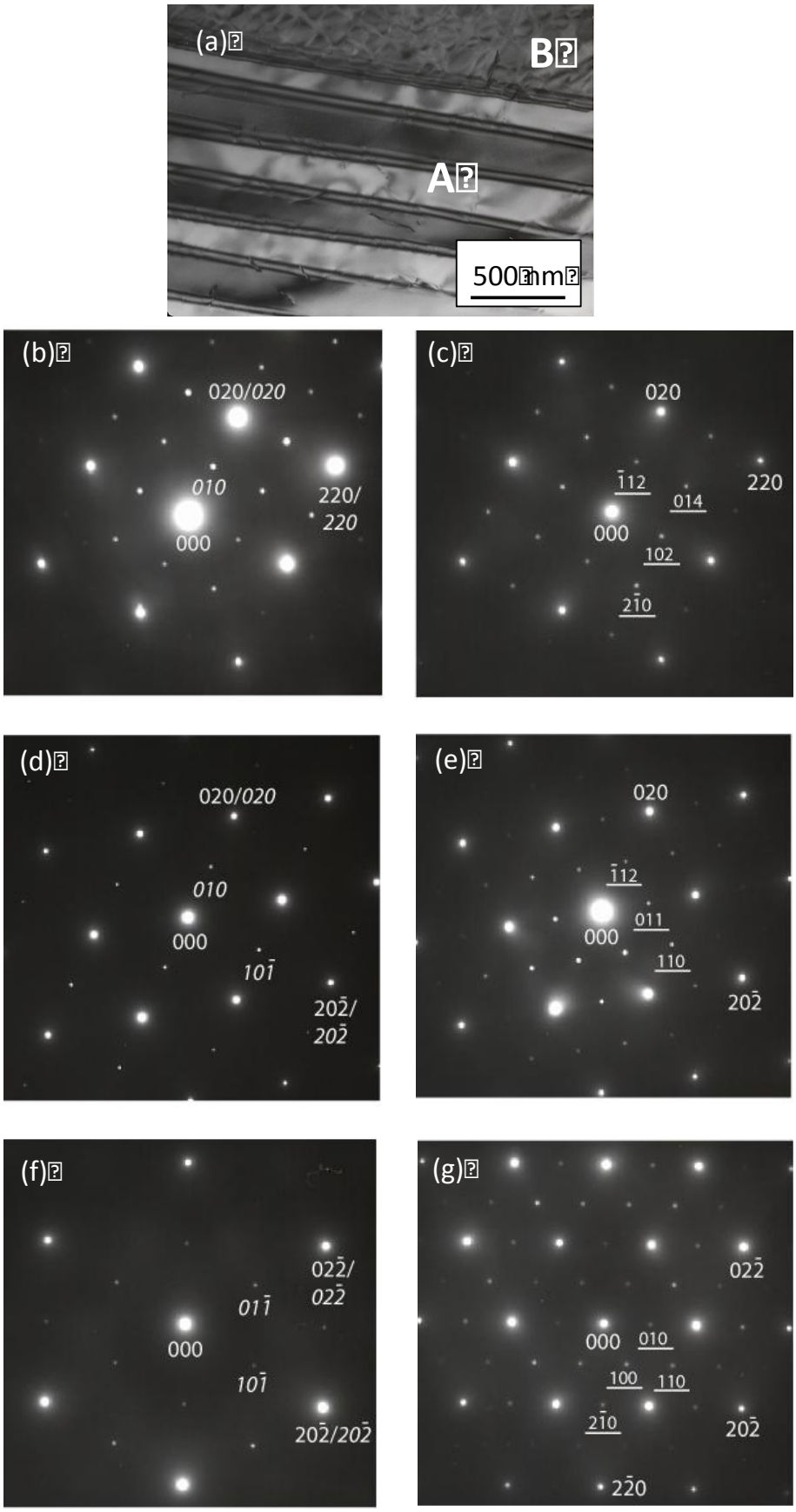
(a)
B
A
500nm
(b)
020/020
010
220/
220
000
(c)
020
$\bar{1}12$
220
014
000
102
$2\bar{1}0$
(d)
020/020
010
000
$10\bar{1}$
$20\bar{2}$/
$20\bar{2}$
(e)
020
$\bar{1}12$
011
000
110
$20\bar{2}$
(f)
$02\bar{2}$/
$02\bar{2}$
$01\bar{1}$
000
$10\bar{1}$
$20\bar{2}/20\bar{2}$
(g)
$02\bar{2}$
000
010
100
110
$2\bar{1}0$
$20\bar{2}$
$2\bar{2}0$

Figure 1

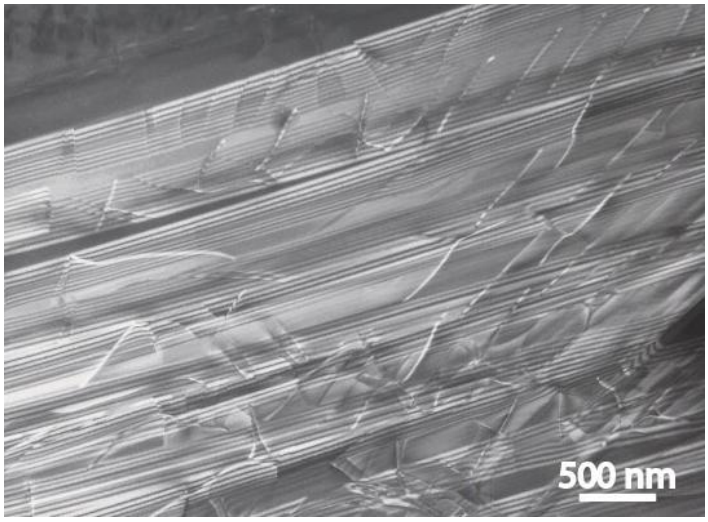

Figure 2

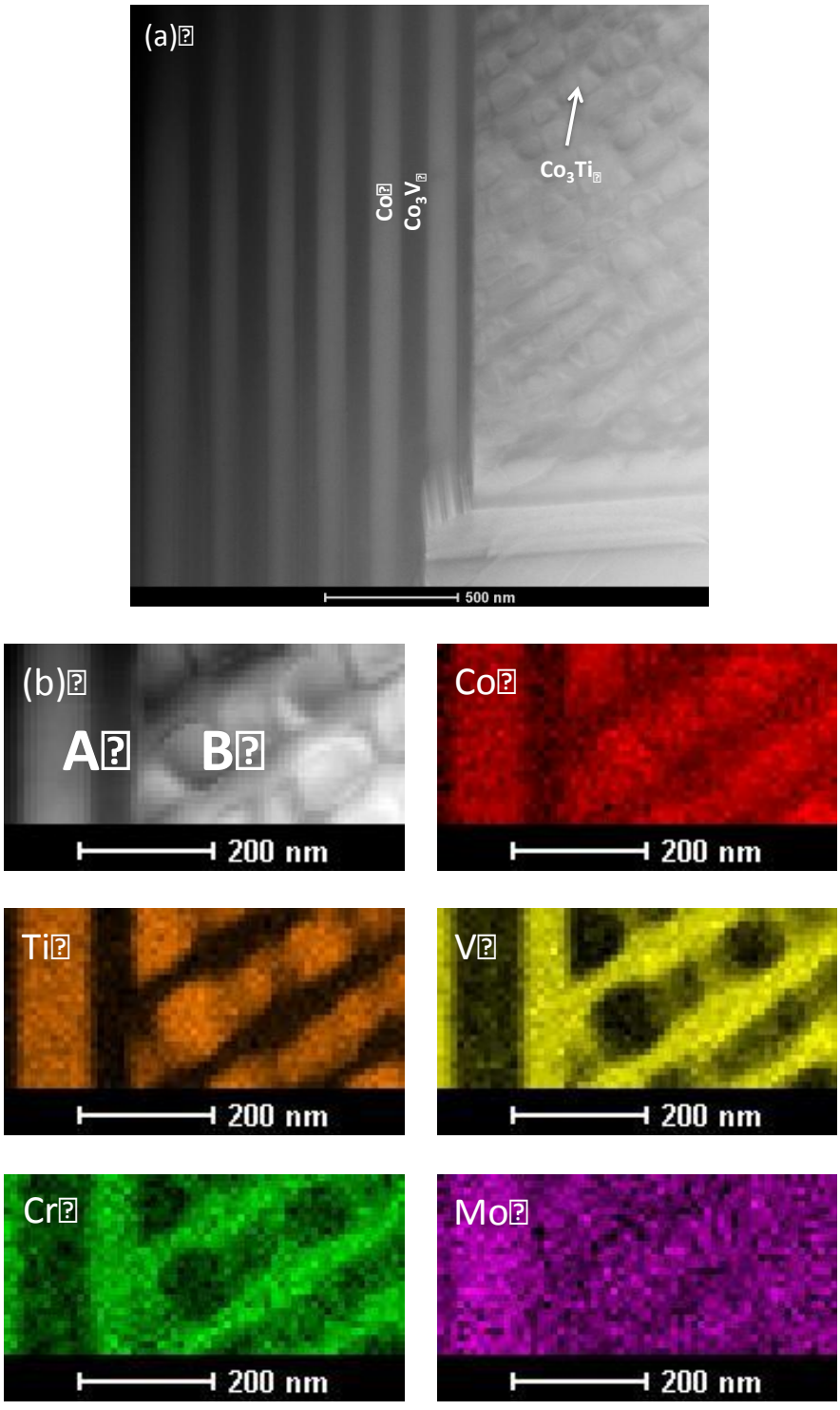
(a)
Co
Co3V
Co3Ti
500 nm
(b)
A
B
200 nm
Co
200 nm
Ti
200 nm
V
200 nm
Cr
200 nm
Mo
200 nm

Figure 3

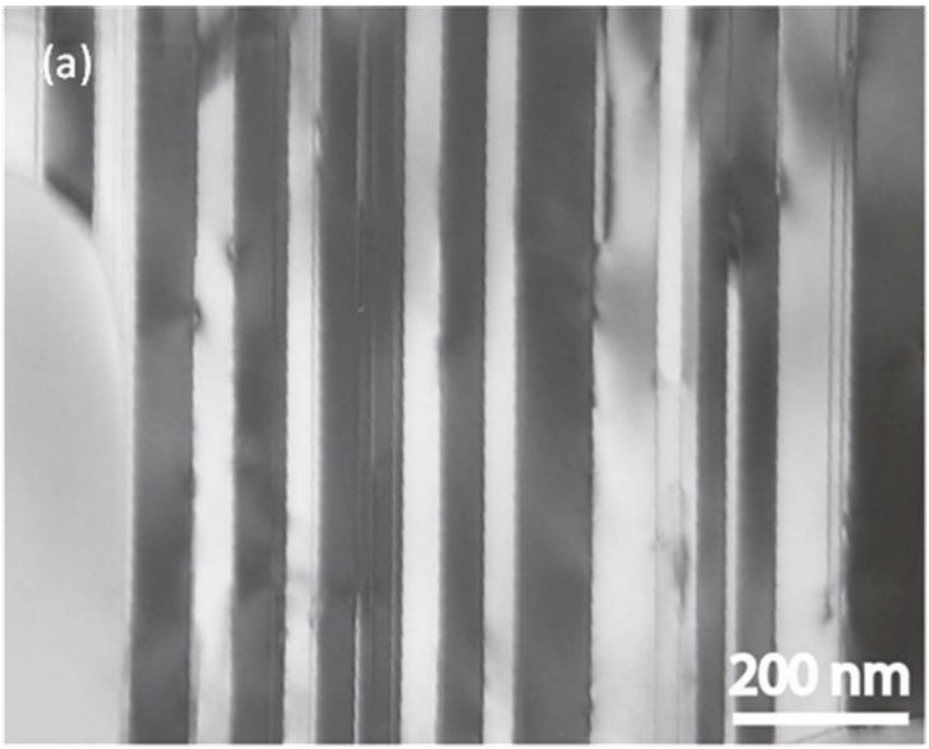

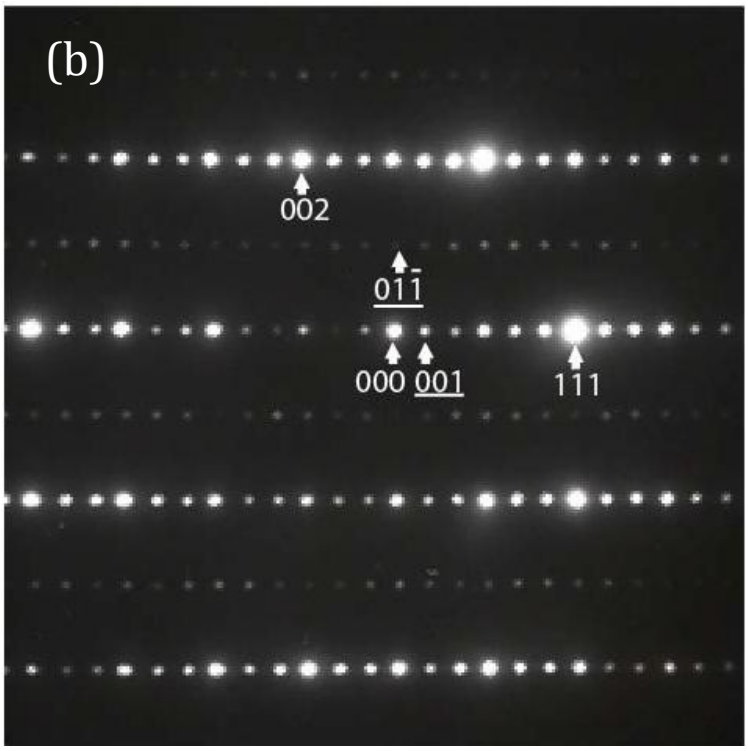

Figure 4

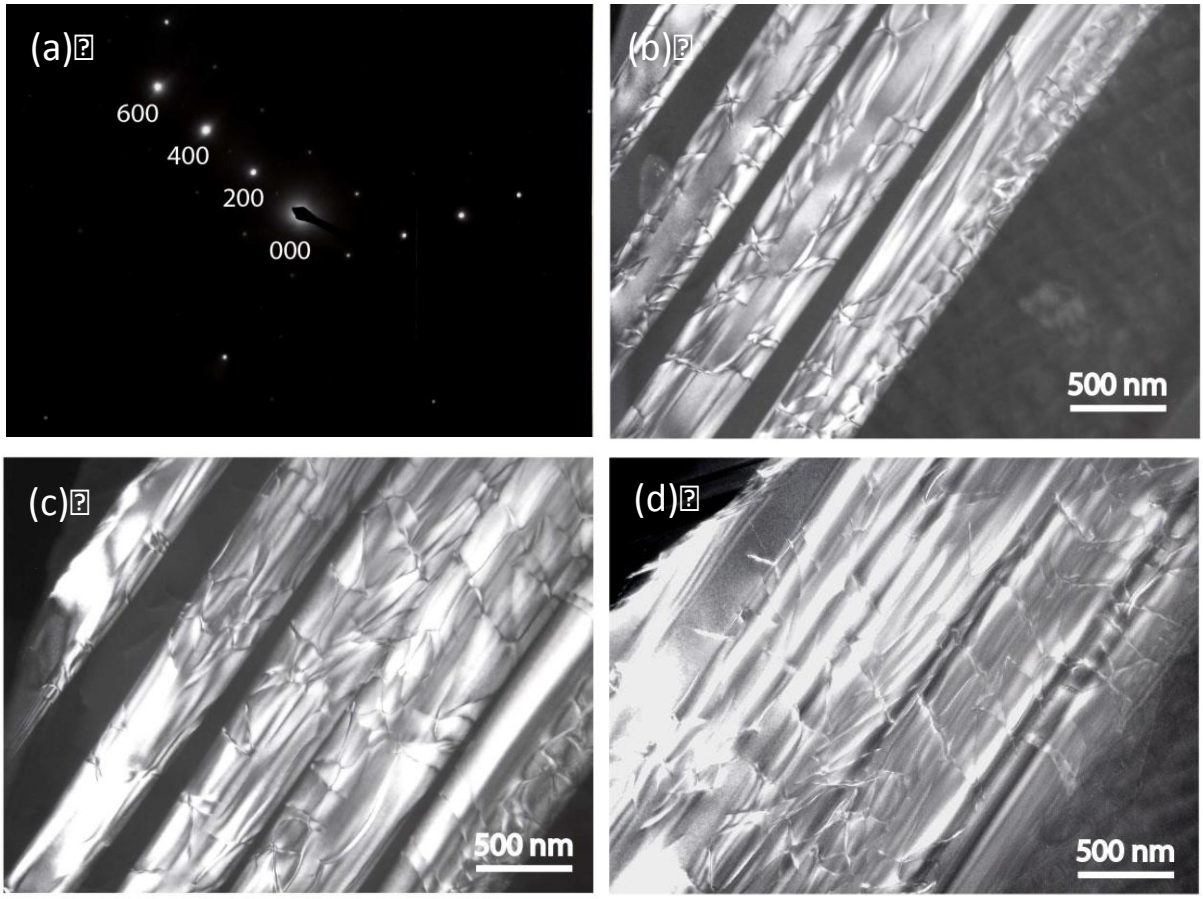

Figure 5